Nanoscale

ROYAL SOCIETY OF CHEMISTRY

PAPER

View Article Online
View Journal | View Issue

Cite this: *Nanoscale*, 2025, **17**, 8588

Magnetically targeted delivery of probiotics for controlled residence and accumulation in the intestine†

Hanye Xing,‡ Xingyu Liu,‡ Ju Wang,* Tao Zhou, Xiangxiang Jin, Rui Qiu, Yang Lu, Changhong Liu * and Yonghong Song *

The effectiveness of orally delivered probiotics in treating gastrointestinal diseases is restricted by inadequate gut retention. In this study, we present a magnetically controlled strategy for probiotic delivery, which enables controlled accumulation and residence of probiotics in the intestine. The magnetically controlled probiotic is established by attaching amino-modified iron oxide (Fe_3O_4–NH_3^+ NPs) to polydopamine-coated *Lacticaseibacillus rhamnosus* GG (LGG@P) through electrostatic self-assembly and named as LGG@P@Fe_3O_4. In a simulated gastrointestinal environment, LGG@P@Fe_3O_4 maintains both structural stability and probiotic viability. Furthermore, the LGG@P@Fe_3O_4 clusters can be easily manipulated by an external magnetic field, inducing directional movement and aggregation. *In vitro* simulations demonstrated significant accumulation and retention of LGG@P@Fe_3O_4 under a magnetic field, with the optical density (OD) value of the suspension decreasing from ~1.17 to ~0.29. In contrast, the OD value of the suspension without a magnetic field remained at its original level (~1.15). In a mouse model with intragastrically administered LGG@P@Fe_3O_4, the group exposed to a magnet exhibited stronger gut fluorescence after 24 h. The magnetically controlled probiotic delivery strategy offers an easy manufacturing and feasible method to enhance the effectiveness of probiotics in treating gastrointestinal diseases.

Received 13th November 2024,
Accepted 22nd February 2025

DOI: 10.1039/d4nr04753b

rsc.li/nanoscale

Introduction

Probiotics are active microorganisms that offer health benefits to humans.[1–3] They play a crucial role in enhancing nutrient absorption by regulating mucosal and systemic immune functions and balancing the gut microbiota.[4–7] These health-promoting characteristics make probiotics promising for preventing and treating various gastrointestinal diseases.[8–11] However, challenges remain regarding the effectiveness of probiotics in treating gastrointestinal diseases, specifically in two aspects: (1) probiotics must withstand harsh gastrointestinal conditions, such as stomach acid and bile, to reach the intestines effectively.[12,13] (2) Constant peristalsis of the gastrointestinal tract limits the colonization ability of probiotics in the intestines and probiotics are rapidly cleared from the gastrointestinal tract, which greatly reduces their bioavailability and therapeutic efficacy.[14,15] Surface functionalization of bacteria is widely employed for protecting the probiotics and can act as a barrier, protecting probiotics from harsh gastrointestinal environments and preserving their bioactivity.[16–20] Consequently, enhancing probiotic retention in the gut is essential to improve therapeutic efficacy.

Various drug delivery systems have been developed to enhance probiotic retention in the gut,[21–23] such as micro-

Anhui Province Key Laboratory of Advanced Catalytic Materials and Reaction Engineering, School of Chemistry and Chemical Engineering, School of Food and Biological Engineering, Hefei University of Technology, Hefei, 230009, China. E-mail: songyh@hfut.edu.cn, changhong22@hfut.edu.cn, orangezi30940@163.com

† Electronic supplementary information (ESI) available. See DOI: https://doi.org/10.1039/d4nr04753b

‡ These authors contributed equally to this work.

Yonghong Song

Yonghong Song is currently an associate professor at the Hefei University of Technology (HFUT). He obtained his B.E. degree in 2015 and his Ph.D. degree in 2020, both from HFUT. He worked as a postdoctoral researcher (2020–2022) at the University of Science and Technology of China (USTC). He has been focusing on the assembly and biomedical applications of magnetic nanomaterials.

device-based sustained release systems,[24,25] mucoadhesive systems,[26,27] and targeted modifications.[28–30] These delivery systems effectively extend the gut retention time.[31,32] However, the scale-up is restricted by complex manufacturing processes and high costs. Developing simple, low-cost, and adaptable probiotic delivery systems is crucial for clinical applications. The magnetic field is a 3D spatial field that is easy to generate and manipulate, offering safety, speed, and precision.[33–35] The magnetic field endows magnetically controlled systems with attractive features, including controllability, safety, non-contact operation, and rapid response, making it widely explored for *in vivo* biomedical applications.[36–40] For example, magnetically controlled ferromagnetic soft robots can navigate through narrow and tortuous vasculature,[41] and magnetically driven capsules can perform targeted drug delivery and sampling in the stomach or intestine.[42] Additionally, magnetic microswarms can enable active endovascular delivery under an external magnetic field.[43] Therefore, introducing a magnetically controlled probiotic delivery system is highly feasible for achieving controlled residence and efficient accumulation in the intestine.

In this study, we developed a magnetically controlled probiotic delivery strategy based on electrostatic interactions between electropositive magnetic nanoparticles and electronegative probiotics. The magnetic probiotic was assembled by polydopamine-modified *Lacticaseibacillus rhamnosus* GG (LGG@P) and amino-modified iron oxide (Fe_3O_4–NH_3^+ NPs), referred to as LGG@P@Fe_3O_4 (Fig. 1a). After exposure to simulated gastric fluid (SGF) and simulated intestinal fluid (SIF), LGG@P@Fe_3O_4 exhibited excellent bacterial viability due to the protective polydopamine coating. Moreover, Fe_3O_4 endows LGG@P@Fe_3O_4 with excellent magnetic properties, enabling it to be attracted by an external magnetic field, leading to enhanced and controlled gut retention after oral administration (Fig. 1b). In the *in vitro* simulation, LGG@P@Fe_3O_4 was effectively entrapped by an external magnet and remained stable during 30 min of washing. Moreover, the manufacturing process of LGG@P@Fe_3O_4 is straightforward and of low cost. Overall, the magnetically controlled probiotic delivery strategy provides an effective, controllable, and versatile approach for the treatment of gastrointestinal diseases, demonstrating high feasibility for clinical applications.

Results and discussion

Preparation and characterization of Fe_3O_4–NH_3^+ NPs

To prepare LGG@P@Fe_3O_4, firstly, positively charged Fe_3O_4–NH_3^+ NPs were prepared using a surface modification procedure using TEOS and APTES (Fig. 2a). The prepared Fe_3O_4 NPs had a spherical shape (Fig. S1a†) with a narrow size distribution (Fig. 2b). After the formation of a silica-coated shell, Fe_3O_4 NPs were functionalized using APTES to obtain Fe_3O_4–NH_3^+ NPs with unchanged morphology (Fig. S1b†). After the successful modification, Fig. 2c shows a TEM image of Fe_3O_4–NH_3^+ NPs with the Fe_3O_4 core coated with the thin shell of silica, which made the initially rough surface of the Fe_3O_4 NPs relatively smooth. Moreover, DLS analysis indicated that the size of Fe_3O_4–NH_3^+ NPs was close to that of uncoated Fe_3O_4 NPs, meaning the modification would not impair their dispersity. In contrast to the negatively charged Fe_3O_4 NPs with ~−35 mV, the Fe_3O_4–NH_3^+ NPs exhibited a positive charge with ~17 mV (Fig. 2e). Furthermore, Fourier transform infrared spectroscopy (FTIR) was used to investigate the successful modification. In Fig. 2f, the peaks at 625 and 580 cm^{-1} demonstrated the presence of the Fe_3O_4 NPs, and the existence of APTES with characteristic amine groups (–NH_3^+) was confirmed by the appearance of peaks at 954, 1065 and

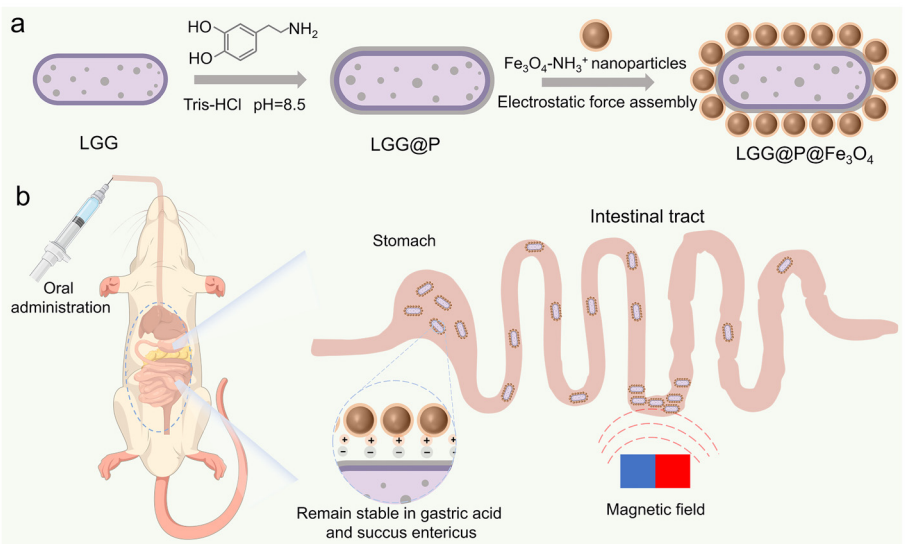

Fig. 1 (a) Schematic illustration of the preparation of LGG@P@Fe_3O_4. (b) Schematic illustration of the magnetically targeted probiotic delivery system and LGG@P@Fe_3O_4 controlled residence and efficient accumulation in the intestine.

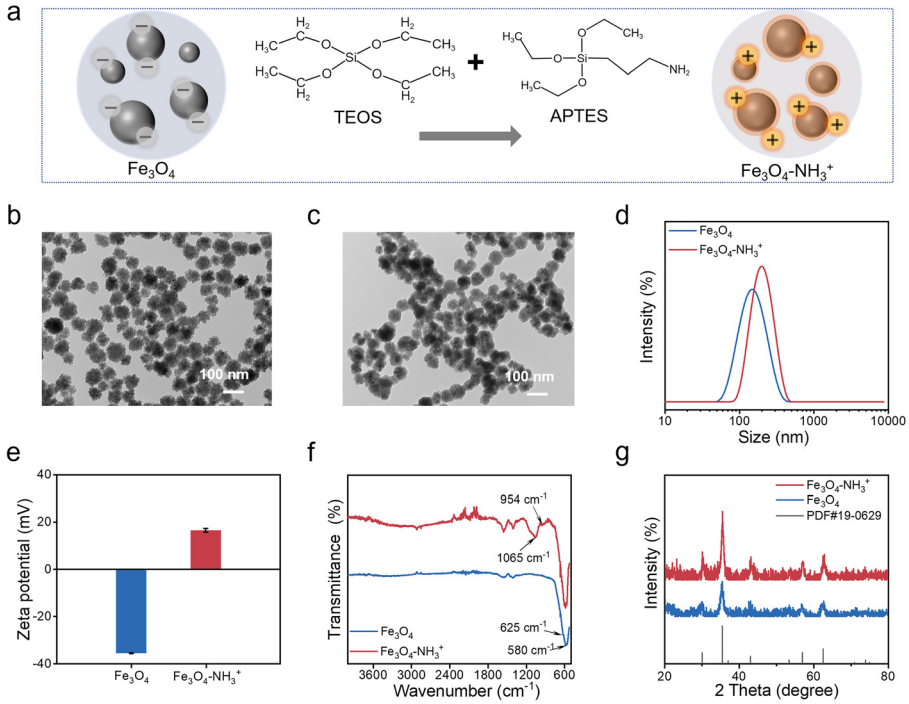

Fig. 2 (a) Schematic illustration of the preparation of Fe_3O_4–NH_3^+ NPs. The TEM images of (b) Fe_3O_4 NPs and (c) Fe_3O_4–NH_3^+ NPs. (d) The hydrodynamic size distribution of Fe_3O_4 and Fe_3O_4–NH_3^+ NPs. (e) Zeta potential values of Fe_3O_4 and Fe_3O_4–NH_3^+ NPs. (f) The FTIR spectra of Fe_3O_4 and Fe_3O_4–NH_3^+ NPs. (g) The XRD patterns of Fe_3O_4 and Fe_3O_4–NH_3^+ NPs.

1547 cm^{-1}, which were respectively assigned to the Si–O, Si–O–Si and N–H stretching. The X-ray photoelectron spectroscopy (XPS) (Fig. S2†) analysis also demonstrated the successful modification. As shown in the X-ray powder diffraction (XRD) patterns (Fig. 2g), the Fe_3O_4 phase existed in both samples, and no other peaks were detected in the Fe_3O_4–NH_3^+ NPs, showing that no crystallinity changes occurred during the modification. Besides, EDS mapping (Fig. S3†) showed the distribution and mass fraction (wt%) of O (~38 wt%), Fe (~58 wt%), and Si (~4 wt%). These results demonstrated that the surface modification successfully grafted the negatively charged Fe_3O_4 NPs to the positively charged Fe_3O_4–NH_3^+ NPs.

Preparation and characterization of LGG@P

We synthesized LGG@P by a facile method of immersing LGG in an aqueous alkaline solution of dopamine according to the previous report.[44] The schematic illustration of LGG@P preparation is shown in Fig. 3a. Dopamine polymerization was carried out in Tris-HCl (pH 8.5), generating a uniform coating on the LGG surface. As shown in Fig. 3b, the color of the suspension changed from milky white (LGG) to gray (LGG@P), indicating the successful formation of a polydopamine coating. TEM images revealed that, compared to LGG (Fig. 3c), LGG@P (Fig. 3d) exhibited a thin polydopamine shell with anchored nanoparticles. Meanwhile, the zeta potential was measured to confirm the formation of the coating. As shown in Fig. 3e, after modification with polydopamine, a significant decrease in the zeta potential of LGG@P (from ~−7 mV to ~−13 mV) was observed. Overall, the changes in suspension color, TEM analysis, DLS analysis (Fig. S4†) and zeta potential measurements confirm successful surface modification, resulting in a protective layer and enhanced negative surface charge.

Preparation and characterization of LGG@P@Fe_3O_4

Subsequently, Fe_3O_4–NH_3^+ NPs and LGG@P served as the positively and negatively charged building blocks in the preparation of LGG@P@Fe_3O_4. As shown in Fig. 4a, the electrostatic interaction resulted in the assembly of Fe_3O_4–NH_3^+ NPs and LGG@P into LGG@P@Fe_3O_4. As shown in Fig. 4b, the presence of Fe_3O_4–NH_3^+ NPs was directly observed in optical images, which showed a color change. To further observe the structure of LGG@P@Fe_3O_4, TEM images (Fig. 4c) revealed that the Fe_3O_4–NH_3^+ NPs were anchored on the surface of LGG@P with uniform distribution. We evaluated changes in the zeta potential of Fe_3O_4–NH_3^+ NPs, LGG@P, and LGG@P@Fe_3O_4. As shown in Fig. 4d, the zeta potential of Fe_3O_4–NH_3^+ NPs was 17.3 mV and that of LGG@P was −12.0 mV, while that of LGG@P@Fe_3O_4 was −8.0 mV after being integrated into LGG@P and Fe_3O_4–NH_3^+ NPs. Furthermore, Fe_3O_4–NH_3^+ NPs endow LGG@P@Fe_3O_4 with excellent magnetic properties. Optical images in Fig. 4e showed that LGG@P@Fe_3O_4 particles were attracted by a magnet. After magnetic attraction, the LGG@P@Fe_3O_4 suspension changed colorless, indicating that LGG@P was enriched together with iron oxide. These results confirmed that

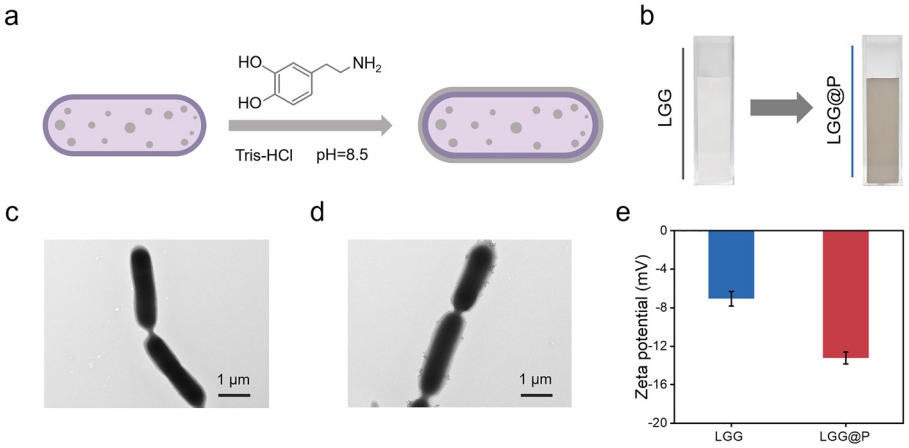

Fig. 3 (a) Schematic illustration of the preparation of LGG@P. (b) The optical images of LGG and LGG@P. (c) TEM image of LGG. (d) TEM image of LGG@P. (e) The zeta potential of LGG and LGG@P.

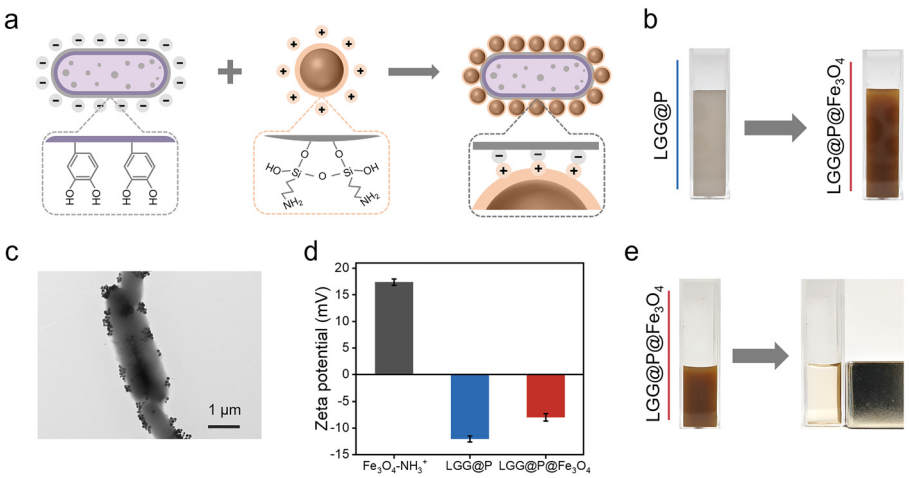

Fig. 4 (a) Schematic illustration of the preparation of LGG@P@Fe_3O_4. (b) The optical images of LGG@P and LGG@P@Fe_3O_4. (c) TEM image of LGG@P@Fe_3O_4. (d) The zeta potential of Fe_3O_4–NH_3^+, LGG@P and LGG@P@Fe_3O_4. (e)The optical images of the samples before and after manipulation by a magnet.

LGG@P@Fe_3O_4 was successfully prepared through electrostatic interactions.

In vitro environmental tolerance

LGG@P@Fe_3O_4 is an oral live biotherapeutic design to produce therapeutic effects in the intestines. During the delivery process, LGG@P@Fe_3O_4 must withstand harsh stomach fluids and maintain a stable structure in intestinal fluids. To investigate the structural stability of LGG@P@Fe_3O_4 in harsh environments, we conducted experiments with various solutions. First, we exposed Fe_3O_4–NH_3^+ NPs, LGG@P, and LGG@P@Fe_3O_4 to various pH conditions and observed changes in the zeta potential. As shown in Fig. 5a, the zeta potential of Fe_3O_4–NH_3^+ NPs increased as the pH decreased, exhibiting a stronger positive charge. The zeta potential of LGG@P increased at pH 2 but remained negative across all pH levels tested (Fig. 5b). Moreover, Fe_3O_4–NH_3^+ NPs and LGG@P still remained stable after 2 h of exposure (Fig. S5†). The results demonstrated that Fe_3O_4–NH_3^+ NPs and LGG@P retained their charge properties under both strongly acidic (pH 2.0) and neutral conditions. When exposed to various pH conditions, Fig. 5c showed that LGG@P@Fe_3O_4 maintained charge stability across these environments. Subsequently, we evaluated the structural stability of LGG@P@Fe_3O_4 in simulated gastric fluid (SGF) and simulated intestinal fluid (SIF) and the results are shown in Fig. 5d–g. The optical images of LGG@P@Fe_3O_4 exposed to SGF (Fig. 5d) and SIF (Fig. 5f) visually confirmed its superior structural stability in harsh environments. As shown in Fig. 5e and g, TEM images revealed that LGG@P@Fe_3O_4 remained structurally intact after exposure to SGF or SIF for 2 h. These results indicated that LGG@P@Fe_3O_4 has superior structural stability, allowing it to withstand harsh gastric and intestinal conditions, thereby enhancing its delivery efficacy.

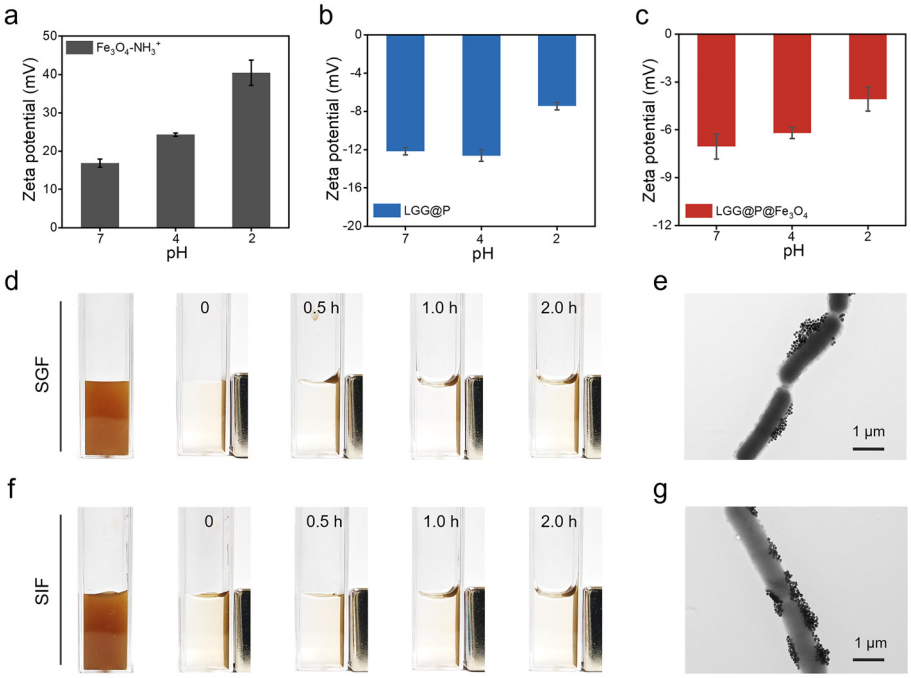

Fig. 5 Zeta potential values at different pH levels. (a) Fe_3O_4–NH_3^+ NPs, (b) LGG@P, and (c) LGG@P@Fe_3O_4. (d) Stability of LGG@P@Fe_3O_4 in SGF. (e) TEM image of LGG@P@Fe_3O_4 after exposure to SGF for 24 h. (f) Stability of LGG@P@Fe_3O_4 in SIF. (g) TEM image of LGG@P@Fe_3O_4 after exposure to SIF for 24 h.

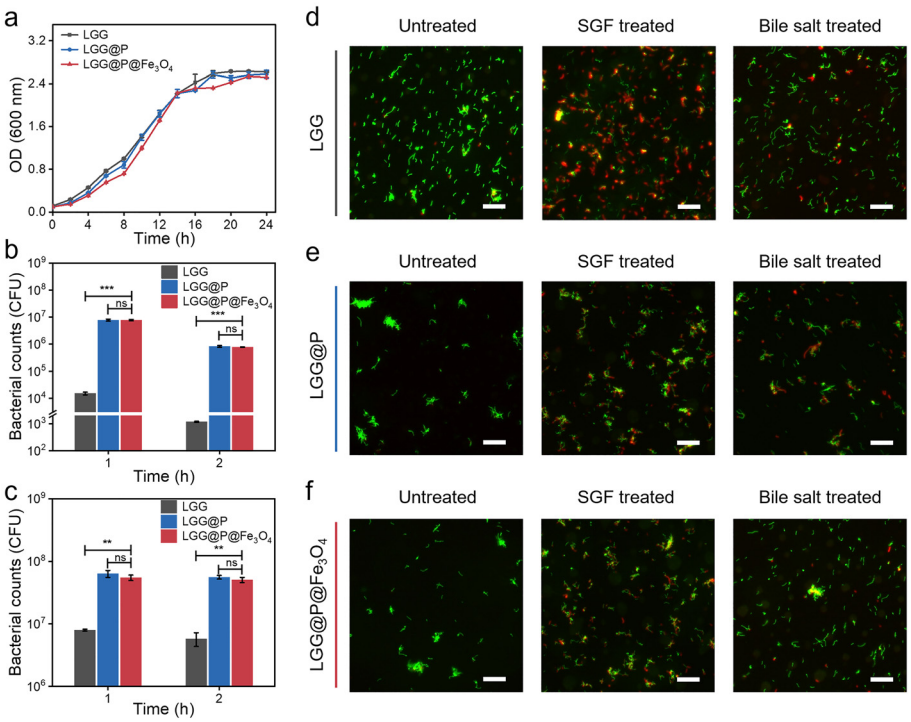

Fig. 6 (a) The growth curves of LGG, LGG@P, and LGG@P@Fe_3O_4. (b) The bacterial counts of LGG, LGG@P, and LGG@P@Fe_3O_4 after exposure to simulated gastric fluid. (c) The bacterial counts of LGG, LGG@P, and LGG@P@Fe_3O_4 after exposure to a bile salt solution. Optical fluorescence microscopy images of the untreated, SGF treated, and bile salt treated samples. The scale bar is 10 μm. (d) LGG, (e) LGG@P, and (f) LGG@P@Fe_3O_4. Data are presented as the means ± SD. * $P < 0.05$, ** $P < 0.01$, *** $P < 0.001$. ns, no significance.

Probiotic activity has a significant impact on the effectiveness of oral live biotherapeutics. To evaluate the viability of LGG after polydopamine coating and Fe_3O_4–NH_3^+ NP adhesion, we measured the bacterial growth curves using optical density (OD) experiments with LGG, LGG@P, and LGG@P@Fe_3O_4. As shown in Fig. 6a, LGG, LGG@P, and LGG@P@Fe_3O_4 exhibited similar growth curves, with no significant differences in OD values at the same incubation times. The impact of coating bacteria with polydopamine on their viability and bioactivity was minimal. The results indicated that polydopamine coating and Fe_3O_4–NH_3^+ NP adhesion had almost no effect on LGG viability. Furthermore, we evaluated the survival of LGG@P@Fe_3O_4 under harsh conditions. The hydrogen ions present in gastric acid can modify the surface permeability of probiotics, leading to cell death.[45] The presence of bile salts can break down lipids and ultimately lead to probiotic death.[46] Specifically, LGG, LGG@P, and LGG@P@Fe_3O_4 with bacterial counts of ~1×10^8 colony forming units (CFU) were exposed to SGF and a bile salt solution. As shown in Fig. 6b, the bacterial count of LGG reached only ~1.5×10^4 CFU after 1 h of SGF exposure. In comparison, the bacterial count remained high for LGG@P (~7.6×10^6 CFU) and LGG@P@Fe_3O_4 (~7.7×10^6 CFU). Compared with LGG (~1.2×10^3 CFU), even after 2 h of exposure, LGG@P (~8.1×10^5 CFU) and LGG@P@Fe_3O_4 (~7.6×10^5 CFU) still exhibited high viability. As shown in Fig. 6c, LGG@P and LGG@P@Fe_3O_4 also exhibited significantly higher viability than LGG after exposure to a bile salt solution. The survival of LGG, LGG@P, and LGG@P@Fe_3O_4 in SGF and a bile salt solution was further investigated using the live/dead cell viability assay. As shown in Fig. 6d, strong green fluorescence signals were observed in the confocal fluorescence images of untreated LGG, indicating an abundance of live bacteria. In contrast, strong red and weak green fluorescence signals appeared in the SGF-treated group, indicating that a large proportion of LGG did not survive. Additionally, strong green and weak red fluorescence signals were observed in the bile salt-treated group, indicating that LGG had a high survival rate. Notably, strong green fluorescence signals were observed in all LGG@P and LGG@P@Fe_3O_4 samples (Fig. 6e and f). These

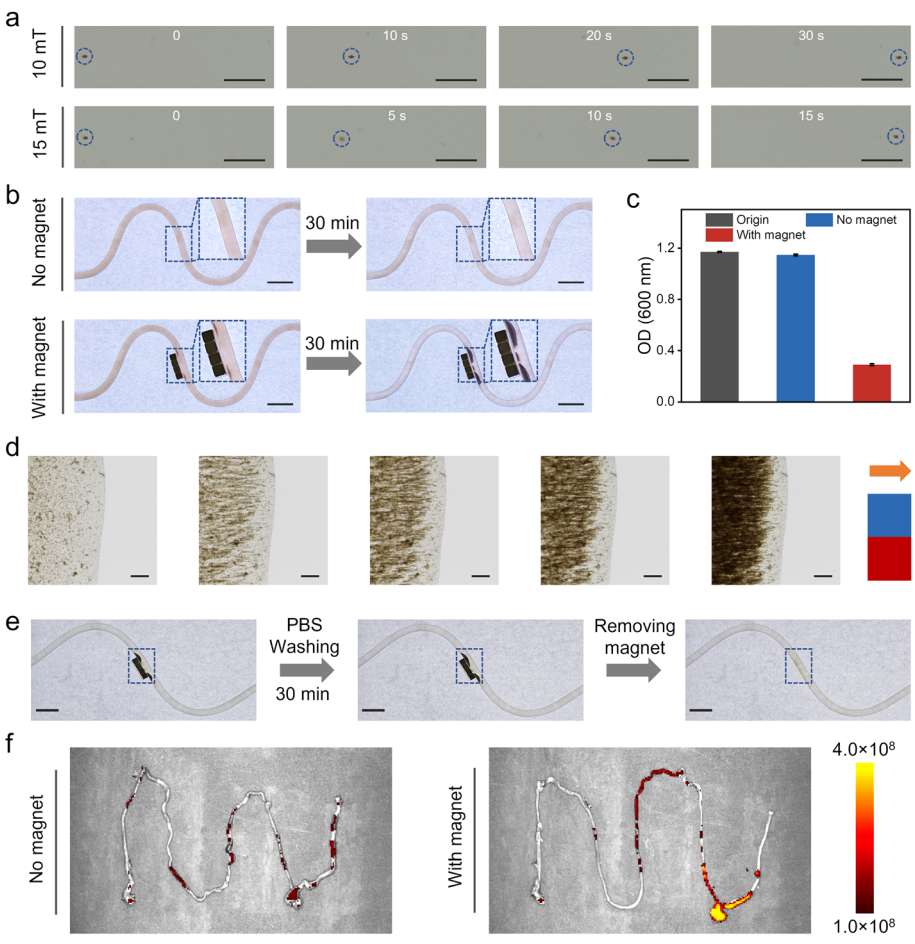

Fig. 7 (a) The magnetically controlled movement process of LGG@P@Fe_3O_4 under a magnetic field. The scale bar is 100 μm. (b) The controlled aggregation of LGG@P@Fe_3O_4 suspension in the presence or absence of a magnet. The scale bar is 2 cm. (c) The OD values of the LGG@P@Fe_3O_4 suspension with different treatments. (d) The magnetic aggregation process of LGG@P@Fe_3O_4 under a magnet. The scale bar is 200 μm. (e) The controlled retention of LGG@P@Fe_3O_4. The scale bar is 2 cm. (f) Fluorescence imaging of intestines at 24 h post-gavage of LGG@P@Fe_3O_4.

results indicated that the polydopamine coating provided excellent protection, allowing LGG@P@Fe_3O_4 to achieve higher survival rates than LGG, thereby enabling more live probiotics to reach the intestines successfully.

Magnetically controlled motion behavior of LGG@P@Fe_3O_4

The magnetically controlled aggregation and retention of LGG@P@Fe_3O_4 were evaluated *in vitro*. Firstly, we investigated whether the magnet had any effect on probiotic activity. As shown in Fig. S6a,† the growth curves of LGG with and without a magnet were similar. The bacterial counts of LGG@P@Fe_3O_4 under SGF with and without the magnet exhibited similar quantities (Fig. S6b†). These results indicated that the impact of the magnetic field on the bioactivity of LGG and LGG@P@Fe_3O_4 was minimal. Subsequently, an optical microscope was employed to observe the movement of LGG@P@Fe_3O_4 in a liquid environment. As shown in Fig. 7a, when the magnetic field intensity was 10 mT, the LGG@P@Fe_3O_4 cluster took 30 s to move to the opposite end, with an approximate movement speed of 14.3 μm s^{-1}. Moreover, when the magnetic field intensity was increased to 15 mT, the movement speed rose to 28.1 μm s^{-1}, and the cluster only required 15 s to cover the same distance. Their observations indicated that LGG@P@Fe_3O_4 can respond to an external magnetic field, producing magnetic field intensity-dependent motion behaviors. Subsequently, a microfluidic device was used to mimic the intestine, and the retention effect of LGG@P@Fe_3O_4 under the magnetic field was evaluated. As shown in Fig. 7b, in the absence of a magnetic field, LGG@P@Fe_3O_4 retention did not occur during circulation flow for 30 min. In contrast, LGG@P@Fe_3O_4 was attracted to the magnet and the surface magnetic field intensity was about 20 mT (Fig. S7†), showing obvious retention. Furthermore, we measured the change in OD values (n = 3) of this process. As shown in Fig. 7c, in the absence of a magnetic field, the OD values did not almost change before (~1.17) and after (~1.15) circulation flow. After being exposed to a magnet, the OD values decreased significantly (from ~1.17 to ~0.29) (Fig. 7c). As shown in Fig. 7d, the aggregation process of LGG@P@Fe_3O_4 was observed. At the original state, LGG@P@Fe_3O_4 particles were randomly dispersed in PBS. When an external magnetic field was applied, LGG@P@Fe_3O_4 moved along the field direction and gradually formed large aggregates. Their observations indicated that LGG@P@Fe_3O_4 can achieve controlled movement and aggregation under an external magnet. We further investigated the magnetically controlled retention stability of LGG@P@Fe_3O_4 by washing with PBS. As shown in Fig. 7e, the accumulation of LGG@P@Fe_3O_4 was retained even after washing for 30 min. The transmittance of the PBS solution remained approximately the same before and after washing (Fig. S8†). After removing the magnet, the accumulated LGG@P@Fe_3O_4 quickly dispersed and was flushed away by PBS. To assess the magnetically controlled retention of LGG@P@Fe_3O_4 *in vivo*, we employed IVIS Spectrum imaging to monitor fluorescence signals (LGG@P@Fe_3O_4 modified with FITC) in the intestines of mice after intragastric administration. Obviously, the intestines of mice treated with a magnet maintained high fluorescence intensity after 24 h, whereas almost no fluorescence signal was detected in the group without a magnet (Fig. 7f), indicating prolonged gut retention by magnetic targeting. These results indicated that LGG@P@Fe_3O_4 possesses excellent magnetic properties, enabling controlled aggregation and retention.

Conclusions

In this work, we reported a magnetically controlled oral therapeutic probiotic delivery system. The system was prepared by the polydopamine-mediated surface modification of LGG (LGG@P) and the surface of amino-functionalized Fe_3O_4 nanoparticles (Fe_3O_4–NH_3^+ NPs), denoted as LGG@P@Fe_3O_4. At different pH levels, LGG@P@Fe_3O_4 exhibited excellent structural stability. Moreover, after being exposed to artificial gastric juice and a bile salt solution, LGG@P@Fe_3O_4 exhibited significantly higher activity than LGG. For the *in vitro* simulation experiment, LGG@P@Fe_3O_4 demonstrated superior magnetic responsiveness. Under an external magnetic field, LGG@P@Fe_3O_4 also demonstrated superior intestinal controlled aggregation and retention compared to LGG. This magnetically controlled delivery system presents a controlled, universal, efficient, and user-friendly delivery strategy for oral live biotherapeutics.

Experimental

Materials

Iron chloride hexahydrate ($FeCl_3{\cdot}6H_2O$), dopamine hydrochloride, tetraethyl orthosilicate (TEOS), and (3-aminopropyl) triethoxysilane (APTES) were obtained from Aladdin Reagent Co. Ltd. Sodium acetate anhydrous (NaAc, ≥99.0%), ethanol, ethylene glycol (EG), and diethylene glycol (DEG) were purchased from Sinopharm Chemical Reagent Co. Ltd. Polyacrylic acid (PAA, MW ≈ 1800 g mol^{-1}) was purchased from Sigma-Aldrich Co. Ltd. 1 M Tris-HCl solution (pH 8.5) was purchased from Sangon Biotech (Shanghai) Co. Ltd. 1× PBS (pH 7.4) was purchased from Wuhan Servicebio Technology Co., Ltd. All chemicals were used without any purification unless otherwise specified.

Characterization

The morphologies of Fe_3O_4 and Fe_3O_4–NH_3^+ NPs were observed under a scanning electron microscope (Zeiss Supra 40, Germany) and a transmission electron microscope (Hitachi HT 7700). X-ray photoelectron spectroscopy (XPS) spectra were recorded using a Thermo ESCALAB250Xi instrument. A Philips X' Pert PRO SUPER (Netherlands) was used to record the X-ray diffraction patterns of the samples. The size and zeta potential were measured by dynamic light scattering (DLS) using a Malvern Zetasizer (Nano-ZS90, UK). The concentrations of Fe_3O_4 and Fe_3O_4–NH_3^+ NPs were measured by inductively

coupled plasma atomic emission spectroscopy (Optima 7300 DV).

Synthesis of Fe_3O_4–NH_3^+ nanoparticles

Fe_3O_4 NPs were synthesized according to the previous report.[47] Ethylene glycol (EG) and diethylene glycol (DEG) were added to a beaker. Then $FeCl_3{\cdot}6H_2O$ (1.08 g), PAA (0.1 g), and NaAc (4.0 g) were dissolved in the above mixture. After stirring for 1 h, the solution was transferred into an autoclave and reacted at 200 °C for 10 h. Fe_3O_4 NPs were obtained *via* centrifugal separation. Subsequently, Fe_3O_4 NPs (0.3 g) were dispersed uniformly in a mixture of ethanol (140 mL), DIW (30 mL), and ammonia (3 mL) with sonication dispersion. 0.1 mL of TEOS and 0.5 mL of APTES in ethanol (10 mL) were added to the above solution at a 0.5 mL min^{-1} rate and stirred for 2 h. Then 0.5 mL of APTES in ethanol was added to the mixture at the same rate and the stirring was continued for an additional 6 h. The mixture was then centrifuged, and the obtained Fe_3O_4–NH_3^+ NPs were stored in water.

Synthesis of LGG@P

To generate a complete polydopamine coating on the LGG surface, a number of 1×10^8 CFU of LGG were gently stirred with 0.8 mg mL^{-1} dopamine in Tris-HCl (pH 8.5) for 30 min at room temperature. The mixture was then centrifuged and washed three times with PBS. The obtained LGG@P was stored in the PBS solution at 4 °C.

Synthesis of LGG@P@Fe_3O_4

To prepare the LGG@P@Fe_3O_4 suspension, 500 μg of Fe_3O_4–NH_3^+ NPs was added to 1 mL of the probiotic suspension containing 1×10^8 CFU of LGG@P and shaken by vortex for thorough mixing in a plastic tube. Then, the mixture was centrifuged and washed three times with PBS. The obtained LGG@P@Fe_3O_4 was stored in the PBS solution at 4 °C.

The growth curve of coated probiotics

A De Man, Rogosa and Sharper (MRS) medium was supplemented with 1 mL of LGG, LGG@P, and LGG@P@Fe_3O_4 and then incubated at 37 °C with shaking at 140 rpm. The OD of the culture was measured at a wavelength of 600 nm every 2 h.

Resistance assay *in vitro*

The strains LGG, LGG@P, and LGG@P@Fe_3O_4, each containing 1×10^8 CFU, were reconstituted in 1 mL of SGF (pH 2.0) or bile salt (0.3 mg mL^{-1}). They were then incubated at 37 °C with shaking at 140 rpm. At 1 h and 2 h time intervals, 100 μL samples from each treatment were taken out and plated on the solid MRS agar for colony counting which was performed after an overnight incubation at 37 °C. Additionally, LGG was stained using a Live & Dead Bacterial Staining Kit and observed using confocal fluorescence images.

In vitro magnetic drive

The magnetically controlled movement ability of LGG@P@Fe_3O_4 was evaluated and observed using an inverted fluorescent microscope (Nikon ECLIPSE Ts2) equipped with a Nikon Digital Sight 10 camera. The magnetic field intensities were 10 and 15 mT.

To evaluate the magnetically controlled aggregation and retention capacity of LGG@P@Fe_3O_4, a silicone tube was fabricated into a microfluidic device. The peristaltic pump was applied to simulate intestinal peristalsis. The magnet was applied to generate the magnetic field.

In vivo magnetic targeting experiment

To evaluate the magnetically controlled aggregation and retention capacity of LGG@P@Fe_3O_4 *in vivo*, LGG@P@Fe_3O_4 was modified by FITC. LGG@P@Fe_3O_4–FITC (~1×10^8 CFU, 300 μL per mouse) was delivered to the stomach of mice by intragastric administration. The mice were then divided into two groups: an experimental group with a fixed magnet placed in the abdomen and a control group that received no treatment. After 24 h of administration, the mice were sacrificed and the intestines were dissected out. Subsequently, the IVIS Spectrum (PerkinElmer) was employed to detect the fluorescence signals within the intestines. All animal experiments were performed following the recommendations in the Guide for the Care and Use of Laboratory Animals of the National Institutes of Health, which were approved by the Institutional Animal Care and Use Committee of Hefei University of Technology (No. HFUT 20250121001M).

Author contributions

Y. H. S. and C. H. L. conceived the idea and designed the experiments. H. Y. X., J. W. and X. Y. L. supervised the research, performed the experiments and analyzed the data. T. Z., X. X. J. and R. Q. helped to analyze the data and provided valuable advice. H. Y. X., J. W., X. Y. L., Y. H. S., C. H. L., and Y. L. co-wrote the manuscript. All authors discussed the results and commented on the manuscript.

Data availability

Additional data are available in the ESI† of this manuscript. The authors will supply the relevant data in response to reasonable requests.

Conflicts of interest

The authors declare no conflicts of interest.

Acknowledgements

This work was financially supported by the National Natural Science Foundation of China (No. 22122502, 51972090, and 22105195), the Fundamental Research Funds for the Central Universities (No. JZ2023HGTB0227, JZ2023YQTD0074, JZ2023HGQB0154, and JZ2024HGQB0092), the Anhui Provincial Natural Science Foundation (2208085MH259), and the Anhui Postdoctoral Scientific Research Program Foundation (2024B810).

References

1 L. C. Beck, A. C. Masi, G. R. Young, T. Vatanen, C. A. Lamb, R. Smith, J. Coxhead, A. Butler, B. J. Marsland, N. D. Embleton, J. E. Berrington and C. J. Stewart, Strain-specific impacts of probiotics are a significant driver of gut microbiome development in very preterm infants, *Nat. Microbiol.*, 2022, **7**, 1525–1535.

2 M. J. Bender, A. C. McPherson, C. M. Phelps, S. P. Pandey, C. R. Laughlin, J. H. Shapira, L. M. Sanchez, M. Rana, T. G. Richie, T. S. Mims, A. M. Gocher-Demske, L. Cervantes-Barragan, S. J. Mullett, S. L. Gelhaus, T. C. Bruno, N. Cannon, J. A. McCulloch, D. A. A. Vignali, R. Hinterleitner, A. V. Joglekar, J. F. Pierre, S. T. M. Lee, D. Davar, H. M. Zarour and M. Meisel, Dietary tryptophan metabolite released by intratumoral Lactobacillus reuteri facilitates immune checkpoint inhibitor treatment, *Cell*, 2023, **186**, 1846–1862.

3 M. E. Sanders, D. J. Merenstein, G. Reid, G. R. Gibson and R. A. Rastall, Probiotics and prebiotics in intestinal health and disease: from biology to the clinic, *Nat. Rev. Gastroenterol. Hepatol.*, 2019, **16**, 605–616.

4 N. Okuka, N. Milinkovic, K. Velickovic, S. Polovina, M. Sumarac-Dumanovic, R. Minic, D. Korcok, B. Djordjevic and N. D. Ivanovic, Beneficial effects of a new probiotic formulation on adipocytokines, appetite-regulating hormones, and metabolic parameters in obese women, *Food Funct.*, 2024, **15**, 7658–7668.

5 J. Wang, L. Wang, S. N. Shi, Y. Q. Cao, J. M. Feng, C. H. Liu and L. Zheng, Probiotic coated with glycol chitosan/alginate relieves oxidative damage and gut dysmotility induced by oxytetracycline in zebrafish larvae, *Food Funct.*, 2022, **13**, 10476–10490.

6 H. J. Zhang, J. P. Zhang, B. Liu, J. Xiao, M. A. C. Stuart, G. H. Hou, H. R. Zhang, S. Liang, Z. K. Li, Q. M. Wang, S. N. Chen, P. L. Li, X. Li and Y. Li, Natural phenolic-metal framework strengthened mesona chinensis polysaccharides microgels for improved viability of probiotics to alleviate the liver injury and gut microbiota dysbiosis, *Adv. Funct. Mater.*, 2024, **34**, 2401064.

7 J. Yang, L. Meng, Y. Li and H. Huang, Strategies for applying probiotics in the antibiotic management of clostridioides difficile infection, *Food Funct.*, 2023, **14**, 8711–8733.

8 P. Guo, W. Wang, Q. Xiang, C. Pan, Y. Qiu, T. Li, D. Wang, J. Ouyang, R. Jia, M. Shi, Y. Wang, J. Li, J. Zou, Y. Zhong, J. Zhao, D. Zheng, Y. Cui, G. Ma and W. Wei, Engineered probiotic ameliorates ulcerative colitis by restoring gut microbiota and redox homeostasis, *Cell Host Microbe*, 2024, **32**, 1502–1518.

9 A. Xie, H. Ji, Z. Liu, Y. Wan, X. Zhang, H. Xiong, S.-P. Nie and H. Wan, Modified prebiotic-based "shield" armed probiotics with enhanced resistance of gastrointestinal stresses and prolonged intestinal retention for synergistic alleviation of colitis, *ACS Nano*, 2023, **17**, 14775–14791.

10 K. Zhang, L. Zhu, Y. Zhong, L. Xu, C. Lang, J. Chen, F. Yan, J. Li, J. Qiu, Y. Chen, D. Sun, G. Wang, K. Qu, X. Qin and W. Wu, Prodrug integrated envelope on probiotics to enhance target therapy for ulcerative colitis, *Adv. Sci.*, 2023, **10**, 2205422.

11 J. Zhou, M. Li, Q. Chen, X. Li, L. Chen, Z. Dong, W. Zhu, Y. Yang, Z. Liu and Q. Chen, Programmable probiotics modulate inflammation and gut microbiota for inflammatory bowel disease treatment after effective oral delivery, *Nat. Commun.*, 2022, **13**, 3432.

12 B.-L. He, R. Cui, T.-G. Hu and H. Wu, Improved viability of probiotics by co-encapsulation of wheat germ oil under storage and gastrointestinal conditions: effects of drying methods and wall composition, *Food Hydrocolloids*, 2025, **158**, 110592.

13 X. Xie, Q. Li, L. Jia, H. Yuan, T. Guo and T. Meng, Multishell colloidosome platform with sequential gastrointestinal resistance for on-demand probiotic delivery, *Adv. Healthcare Mater.*, 2023, **12**, 2202954.

14 S. S. Lin, S. Mukherjee, J. J. Li, W. L. Hou, C. Pan and J. Y. Liu, Mucosal immunity-mediated modulation of the gut microbiome by oral delivery of probiotics into Peyer's patches, *Sci. Adv.*, 2021, **7**, eabf0677.

15 J. Suez, N. Zmora, E. Segal and E. Elinav, The pros, cons, and many unknowns of probiotics, *Nat. Med.*, 2019, **25**, 716–729.

16 M. Chen, L. Xia, C. Wu, Z. Wang, L. Ding, Y. Xie, W. Feng and Y. Chen, Microbe-material hybrids for therapeutic applications, *Chem. Soc. Rev.*, 2024, **53**, 8306–8378.

17 Y. Chen, S. Lin, L. Wang, Y. Zhang, H. Chen, Z. Fu, M. Zhang, H. Luo and J. Liu, Reinforcement of the intestinal mucosal barrier via mucus-penetrating PEGylated bacteria, *Nat. Biomed. Eng.*, 2024, **8**, 823–841.

18 L. J. Fu, Q. He, X. Y. Lu, L. Hu, H. S. Qiang and P. Pei, Surface engineering on bacteria for tumor immunotherapy: strategies and perspectives, *Adv. Funct. Mater.*, 2024, **34**, 2405304.

19 H. H. Li, P. Pei, Q. He, X. X. Dong, C. H. Zhang, W. H. Shen, H. Chen, L. Hu, Y. G. Tao and K. Yang, Nanozyme-coated bacteria hitchhike on $CD11b^{+}$ immune cells to boost tumor radioimmunotherapy, *Adv. Mater.*, 2024, **36**, 2309332.

20 Z. Cao and J. Liu, Coated bacteria: Advanced living materials for microbial therapy, *Acc. Mater. Res.*, 2024, **5**, 872–883.

21 Y. Luo, C. De Souza, M. Ramachandran, S. L. Wang, H. X. Yi, Z. Ma, L. W. Zhang and K. Lin, Precise oral delivery systems for probiotics: a review, *J. Controlled Release*, 2022, **352**, 371–384.
22 D. A. Naik, S. Matonis, G. Balakrishnan and C. J. Bettinger, Intestinal retentive systems - recent advances and emerging approaches, *J. Mater. Chem. B*, 2023, **12**, 64–78.
23 S. Razavi, S. Janfaza, N. Tasnim, D. L. Gibson and M. Hoorfar, Microencapsulating polymers for probiotics delivery systems: preparation, characterization, and applications, *Food Hydrocolloids*, 2021, **120**, 106882.
24 A. Ghosh, L. Li, L. Xu, R. P. Dash, N. Gupta, J. Lam, Q. Jin, V. Akshintala, G. Pahapale, W. Liu, A. Sarkar, R. Rais, D. H. Gracias and F. M. Selaru, Gastrointestinal-resident, shape-changing microdevices extend drug release in vivo, *Sci. Adv.*, 2020, **6**, eabb4133.
25 A. Ren, J. R. Hu, C. W. Qin, N. Xia, M. F. Yu, X. B. Xu, H. Y. Yang, M. Han, L. Zhang and L. Ma, Oral administration microrobots for drug delivery, *Bioact. Mater.*, 2024, **39**, 163–190.
26 Z. Y. Han, C. Zhang, J. X. An, J. Y. Qiao and X. Z. Zhang, Microalgal biomass-assisted delivery of probiotics for modulation of gut homeostasis and alleviation of intestinal inflammation, *Nano Today*, 2024, **54**, 102093.
27 L. M. Zhu, T. T. Yu, W. C. Wang, T. Xu, W. J. Geng, N. Li and X. J. Zan, Responsively degradable nanoarmor-assisted super resistance and stable colonization of probiotics for enhanced inflammation-targeted delivery, *Adv. Mater.*, 2024, **36**, 2308728.
28 A. K. Brodel, L. H. Charpenay, M. Galtier, F. J. Fuche, R. Terrasse, C. Poquet, J. Havranek, S. Pignotti, A. Krawczyk, M. Arraou, G. Prevot, D. Spadoni, M. T. N. Yarnall, E. M. Hessel, J. Fernandez-Rodriguez, X. Duportet and D. Bikard, In situ targeted base editing of bacteria in the mouse gut, *Nature*, 2024, **632**, 877–884.
29 M. K. Heavey, A. Hazelton, Y. Wang, M. Garner, A. C. Anselmo, J. C. Arthur and J. Nguyen, Targeted delivery of the probiotic saccharomyces boulardii to the extracellular matrix enhances gut residence time and recovery in murine colitis, *Nat. Commun.*, 2024, **15**, 3784.
30 Y. Liu, B. Liu, D. Li, Y. Hu, L. Zhao, M. Zhang, S. Ge, J. Pang, Y. Li, R. Wang, P. Wang, Y. Huang, J. Huang, J. Bai, F. Ren and Y. Li, Improved gastric acid resistance and adhesive colonization of probiotics by mucoadhesive and intestinal targeted konjac glucomannan microspheres, *Adv. Funct. Mater.*, 2020, **30**, 2001157.
31 J. Wang, L. Wang, Q. Wang, C. Liu and L. Zheng, Lacticaseibacillus rhamnosus GG enhances fin regeneration under oxytetracycline exposure via activating Wnt signaling and modulating gut microbiota, *Fish Shellfish Immunol.*, 2023, **142**, 109155.
32 X. Yang, J. Yang, Z. Ye, G. Zhang, W. Nie, H. Cheng, M. Peng, K. Zhang, J. Liu, Z. Zhang and J. Shi, Physiologically inspired mucin coated escherichia coli nissle 1917 enhances biotherapy by regulating the pathological microenvironment to improve intestinal colonization, *ACS Nano*, 2022, **16**, 4041–4058.
33 Q. Cao, Q. Fan, Q. Chen, C. Liu, X. Han and L. Li, Recent advances in manipulation of micro- and nano-objects with magnetic fields at small scales, *Mater. Horiz.*, 2020, **7**, 638–666.
34 S. Del Sol-Fernandez, P. Martinez-Vicente, P. Gomollon-Zueco, C. Castro-Hinojosa, L. Gutierrez, R. M. Fratila and M. Moros, Magnetogenetics: remote activation of cellular functions triggered by magnetic switches, *Nanoscale*, 2022, **14**, 2091–2118.
35 T. Q. Xu, J. C. Zhang, M. Salehizadeh, O. Onaizah and E. Diller, Millimeter-scale flexible robots with programmable three-dimensional magnetization and motions, *Sci. Rob.*, 2019, **4**, eaav4494.
36 R. Dreyfus, Q. Boehler, S. Lyttle, P. Gruber, J. Lussi, C. Chautems, S. Gervasoni, J. Berberat, D. Seibold, N. Ochsenbein-Kolble, M. Reinehr, M. Weisskopf, L. Remonda and B. J. Nelson, Dexterous helical magnetic robot for improved endovascular access, *Sci. Rob.*, 2024, **9**, eadh0298.
37 D. Quashie Jr., P. Benhal, Z. Chen, Z. H. Wang, X. L. Mu, X. X. Song, T. Jiang, Y. K. Zhong, U. K. Cheang and J. Ali, Magnetic bio-hybrid micro actuators, *Nanoscale*, 2022, **14**, 4364–4379.
38 Y. Song, Y. Zhu, K. Jiang, X. Liu, L. Dong, D. Li, S. Chen, H. Xing, X. Yan, Y. Lu, X. Yang, J. Wang and Y. Xu, Self-assembling ferrimagnetic fluorescent micelles for bioimaging guided efficient magnetic hyperthermia therapy, *Nanoscale*, 2023, **15**, 365–375.
39 M. Sun, K. Chan, Z. Zhang, L. Wang, Q. Wang, S. Yang, S. Chan, P. Chiu, J. Sung and L. Zhang, Magnetic Microswarm and Fluoroscopy-Guided Platform for Biofilm Eradication in Biliary Stents, *Adv. Mater.*, 2022, **34**, 2201888.
40 Y. Zhu, Y. Song, Z. Cao, L. Dong, Y. Lu, X. Yang and J. Wang, Magnetically actuated active deep tumor penetration of deformable large nanocarriers for enhanced cancer therapy, *Adv. Funct. Mater.*, 2021, **31**, 2103655.
41 Y. Kim, G. A. Parada, S. D. Liu and X. H. Zhao, Ferromagnetic soft continuum robots, *Sci. Rob.*, 2019, **4**, eaax7329.
42 Y. Sun, W. Zhang, J. Gu, L. Xia, Y. Cao, X. Zhu, H. Wen, S. Ouyang, R. Liu, J. Li, Z. Jiang, D. Cheng, Y. Lv, X. Han, W. Qiu, K. Cai, E. Song, Q. Cao and L. Li, Magnetically driven capsules with multimodal response and multifunctionality for biomedical applications, *Nat. Commun.*, 2024, **15**, 1839.
43 Q. Wang, Q. Wang, Z. Ning, K. F. Chan, J. Jiang, Y. Wang, L. Su, S. Jiang, B. Wang, B. Y. M. Ip, H. Ko, T. W. H. Leung, P. W. Y. Chiu, S. C. H. Yu and L. Zhang, Tracking and navigation of a microswarm under laser speckle contrast imaging for targeted delivery, *Sci. Rob.*, 2024, **9**, eadh1978.
44 L. Wang and J. Y. Liu, Dopamine polymerization-mediated surface functionalization toward advanced bacterial therapeutics, *Acc. Chem. Res.*, 2024, **57**, 945–956.

45 X. Wang, Z. Cao, M. Zhang, L. Meng, Z. Ming and J. Liu, Bioinspired oral delivery of gut microbiota by self-coating with biofilms, *Sci. Adv.*, 2020, **6**, eabb1952.
46 A. C. Anselmo, K. J. McHugh, J. Webster, R. Langer and A. Jaklenec, Layer-by-layer encapsulation of probiotics for delivery to the microbiome, *Adv. Mater.*, 2016, **28**, 9486–9490.
47 P. Rana, R. Gaur, R. Gupta, G. Arora, A. Jayashree and R. K. Sharma, Cross-dehydrogenative $C(sp^3)$-$C(sp^3)$ coupling via C-H activation using magnetically retrievable ruthenium-based photoredox nanocatalyst under aerobic conditions, *Chem. Commun.*, 2019, **55**, 7402–7405.